NACA

RESEARCH MEMORANDUM

LONGITUDINAL STABILITY AND DRAG CHARACTERISTICS AT MACH

NUMBERS FROM 0.70 TO 1.37 OF ROCKET-PROPELLED MODELS

HAVING A MODIFIED TRIANGULAR WING

By Rowe Chapman, Jr. and John D. Morrow

Langley Aeronautical Laboratory
Langley Field, Va.

NATIONAL ADVISORY COMMITTEE
FOR AERONAUTICS

WASHINGTON
May 2, 1952

wave pattern. The method was developed and presented in the initial
report of the general program (reference 1). Drag data are obtained
by analysis of the accelerations of the model using the technique pre-
sented in detail in reference 2.

Presented herein are the results of flight tests of a longitudinal-
stability model and a zero-lift-drag model, both having a modified tri-
angular wing of aspect ratio 2.53, a 3.7-percent-thick airfoil at the
root section, and a 5.98-percent-thick airfoil at the tip. The wing
design incorporated a round leading edge, a finite tip chord, and a
swept trailing edge in an attempt to improve wing performance by real-
izing leading-edge suction and better lift characteristics. Basic
aerodynamic parameters that define the longitudinal stability, control
effectiveness, and drag characteristics are presented for a Mach number
range from 0.70 to 1.37.

The models were flown at the Langley Pilotless Aircraft Research
Station, Wallops Island, Va.

SYMBOLS

C_N normal-force coefficient $\left(\dfrac{a_n}{g} \dfrac{W}{qS} \right)$

C_c chord-force coefficient $\left(\dfrac{-a_l}{g} \dfrac{W}{qS} \right)$

C_L lift coefficient $\left(C_N \cos \alpha - C_c \sin \alpha \right)$

C_D drag coefficient $\left(C_c \cos \alpha + C_N \sin \alpha \right)$

$C_{D_{min}}$ minimum drag coefficient

C_m pitching-moment coefficient

a_n normal acceleration as obtained from accelerometer, feet
    per second per second

a_l longitudinal acceleration as obtained from accelerometer,
    positive forward, feet per second per second

W model weight

g acceleration due to gravity, feet per second per second

p   free-stream static pressure, pounds per square foot

V   velocity, feet per second

q   dynamic pressure $\left(\frac{1}{2}\gamma p M^2\right)$

M   Mach number

γ specific-heat ratio (1.40)

S   wing area (including the area enclosed within the fuselage), square feet

R   Reynolds number, based on wing mean aerodynamic chord

$\bar{c}$ wing mean aerodynamic chord, feet

θ angle of pitch, radians

α angle of attack, degrees

δ horizontal-tail deflection, degrees

P   period of pitching oscillation, seconds

t   time, seconds

$T_{1/2}$ time to damp to one-half amplitude, seconds

$C_{L_{opt}}$ lift coefficient for maximum ratio of lift to drag

Subscripts:

T trim

$\dot{\alpha} = \dfrac{d\alpha}{dt}\dfrac{\bar{c}}{2V}\dfrac{1}{57.3}$

$q = \dfrac{d\theta}{dt}\dfrac{\bar{c}}{2V}$

$\theta = \dfrac{d\theta}{dt}$

1   low-range instrument

2   high-range instrument

The symbols $\dot{\alpha}$, α, δ, and q used as subscripts indicate the derivative of the quantity with respect to the subscript; for example,

$$C_{L_\alpha} = \frac{dC_L}{d\alpha}.$$

MODELS AND APPARATUS

Models

Figure 1 shows a drawing of the airplane-configuration-type model used for the longitudinal-stability investigation. The zero-lift-drag model was a symmetrical model with no movable control surfaces as shown in figure 2. Both the longitudinal-stability model and the zero-lift-drag model were flown with the modified triangular wing shown in figure 3. Photographs of the stability model are shown in figure 4 and photographs of the drag model are shown in figure 5. The following letter symbols are used throughout this paper to designate the models:

Model designation	Description
A	Longitudinal-stability model
B	Zero-lift-drag model

The fuselage of model A was composed of a cylindrical center body with converging forward and aft sections to form a closed body of revolution. Reference 3 gives a complete description of the fuselage and control surfaces of the stability model. Model A had a weight of 121.5 pounds and a moment of inertia about the axis of pitch of 12.29 slug-feet^2, and the center of gravity was located at 13.2 percent of the mean aerodynamic chord. The movable horizontal tail surface was deflected by a hydraulic control system programmed to give an approximate square wave pattern of 2.07° and 1.99° deflections.

The fuselage of model B was a body of revolution whose contour can be described by two parabolic-arc segments with vertices that join and

have a common tangent at the point of maximum thickness. Maximum body diameter was located at 40 percent of body length.

Model A had a solid duralumin wing and the wing of model B was constructed of wood with metal inserts. The detail wing design, shown in nondimensional form in figure 3, embodies the following character- istics: The position of the 3.7-percent maximum root thickness was forward at the 18.5 percent chord to give a round-nose airfoil section. Thickness increased to 5.98 percent at 30.0 percent chord at the tip to provide room for structure and control mechanism. Sufficient trailing-edge angle was used to provide thickness at the trailing edge for structure and controls. The leading-edge sweep was 57.08° to keep the leading edge subsonic to a Mach number of above 1.5. A trailing- edge sweep was provided to increase the aspect ratio while not basically departing from the triangular wing. Geometric characteristics of the two models are given in the following table:

Stability-model wing:
    Aspect ratio 2.53
    Area (including fuselage), square feet 3.14
    Area (exposed), square feet 2.08
    Mean aerodynamic chord, feet 1.37
    Span, feet 2.82
    Ratio of maximum fuselage diameter to wing span 0.207
    Ratio of maximum fuselage cross-sectional area
        to wing area 0.0851

Drag-model wing:
    Aspect ratio 2.53
    Area (including fuselage), square feet 30.34
    Area (exposed), square feet 24.80
    Mean aerodynamic chord, feet 4.24
    Span, feet 8.76
    Ratio of maximum fuselage diameter to wing span 0.1236
    Ratio of maximum fuselage cross-sectional area
        to wing area 0.0304

Instrumentation

Model A was equipped with an eight-channel telemeter to transmit data from the model during flight. Measurements recorded were two normal accelerations, longitudinal acceleration, transverse acceleration, control position, angle of attack, total head pressure, and static pressure from a calibrated body orifice. The two normal accelerations were measured by accelerometers of different ranges and hence different sensitivities. The vane-type angle-of-attack indicator was mounted on a sting protruding from the nose of the model.

Model B contained a four-channel telemeter. The measurements transmitted during flight were three longitudinal accelerations and base pressure. Two accelerometers measured accelerations during the coasting period of flight; the third accelerometer measured acceleration during the thrusting period.

Tracking radar units were used for obtaining model range and elevation. Fixed and manually operated 16-millimeter motion-picture cameras were used to photograph the model on launcher, launching of model, and the first portion of the flight. Doppler velocimeter radar provided velocity checks and radiosondes were used to obtain the atmospheric conditions at the time flights were made.

TEST AND ANALYSIS

Test

The longitudinal-stability model was fired at an elevation of approximately 45° from a standard crutch-type launcher as shown in figure 6. Model A had no sustainer rocket and was boosted to maximum velocity by a 6-inch-diameter ABL Deacon rocket motor. A drag separation of model from booster followed booster burnout.

The zero-lift-drag model was launched at an elevation of approximately 70° from a mobile launcher. A detail description of launching procedure is given in reference 4. Model B was accelerated to peak velocity by a 6-inch-diameter ABL Deacon rocket motor which was housed in the fuselage of the model.

All instruments were continuously recording; hence, measurements were taken during both power-on and power-off portions of the flight. The data were analyzed only for the power-off portion of the flight, with the exception of the pressure data. A rate-of-rotation correction was applied to indicated angle of attack to obtain angles at the model center of gravity (reference 5). Tracking radar failed to obtain flight-path data for model A; however, the Doppler radar obtained velocity data at intermittent intervals during both the boosted and free-flight portions of the flight. Good results for both flight path and velocity were obtained from radar for model B.

Figure 7 shows the scale of test for the two models by plots of Reynolds number as a function of Mach number for each flight. Data were obtained for a Mach number range of 0.70 to 1.37 for the tests.

Elevator deflections of 2.07° and -1.99°, pulsed at a rate of 0.578 cycle per second in an approximate square wave pattern, were used for the stability model.

Analysis

Following each horizontal-tail movement, model A experienced a short-period transient oscillation while the horizontal tail remained fixed. Analysis of the period, damping characteristics, and trim values of the appropriate measured quantities using the equations of motion for two degrees of freedom yields the desired aerodynamic parameters. A detailed presentation of this method of analysis is made in appendix A of reference 1.

The data from the models were recorded continuously on the telemeter record for all channels of information. For the purpose of plotting and reduction of data, readings from the telemeter record of the stability model were made at intervals of 0.01 second on the first

1 or $1\frac{1}{2}$ cycles of each oscillation. All slopes were taken from plots

of the data read at 0.01 second. Periods, damping, and trim characteristics are from plots throughout the oscillation. Data reduction for the zero-lift-drag model was accomplished at intervals of 0.01 second in the drag-break region and 0.1 second in smooth regions of the record.

For model A, transient oscillations in the longitudinal plane were normally damped for the high angle-of-attack range. For the low angle-of-attack range the model experienced a damped transverse oscillation. In some instances, primarily at subsonic speeds, when the model experienced the transverse disturbance the normally damped characteristics of the transient oscillation in the longitudinal plane were completely destroyed and the model exhibited no ordered behavior. Analysis, using the methods of reference 1, could not be sensibly utilized on oscillations such as these since the original differential equations were linearized to effect separation of the lateral and longitudinal motions.

ACCURACY

Previous experience has shown the accuracy of telemetered measurements to be ±1 percent of full-scale calibrated range of the instrument. Table I gives the full-scale range of the instruments as well as 1 percent of the full-scale calibrated instrument ranges.

Figure 8 shows the values of measured normal acceleration from the high-range accelerometer plotted against values of normal acceleration

from the low-range accelerometer. The data plotted are taken from the vicinity of peaks of the oscillations in order to minimize errors due to reading accuracy. Using the method of least squares the intercept for A_{n_2}/g was 0.0364 and the slope of the line was 1.0153. The slope and intercept, when compared with those of the 45° line of perfect correlation, are an indication of the repeatability of the measurements. The reading accuracy was obtained from a sampling of 400 points by reading the width between reference lines. These lines were placed on the record by lights spaced a constant distance apart. The sampling showed the reading to have a probable error of 0.0055 inch. This reading error translated into quantities using typical slopes of quantity as a function of deflection is shown in table I.

The 1-percent full-scale error in measured quantities shown in table I translated into coefficient form for typical Mach numbers is:

Stability model		
M	ΔC_D	ΔC_L
0.80	±0.0051	±0.014
1.30	±0.0017	±0.005

Drag model	
M	ΔC_D
0.80	±0.0010
1.30	±0.0005

Additional errors may be present in plotted coefficients due to errors in Mach number and errors in dynamic pressure. Absolute errors in Mach number of approximately 2 percent at subsonic speeds and 1 percent at supersonic speeds are possible. The use of Mach number in computing dynamic pressure increases the possible percentage error for dynamic pressure to approximately five-halves of the percentage error in Mach number.

RESULTS AND DISCUSSION

Lift

The typical variation of lift coefficient with angle of attack is shown in figure 9 for various Mach numbers in the subsonic, transonic, and supersonic ranges. A linear variation of C_L with α is shown for the range of lift coefficients covered by the test. Experimental points are presented to demonstrate the loop or hysteresis effect that lift coefficient plotted as a function of angle of attack exhibits for increasing and decreasing α. Scatter of the points is not severe except for the lower subsonic Mach number where the hysteresis becomes more pronounced. For the elevator deflection -1.99° and $M = 0.70$ a solid line is drawn through the C_L points for decreasing angle of attack and a dashed line through the points for increasing angle of attack. The two separate lines are drawn in this case to demonstrate the reliability of the slopes even though the absolute magnitude of the points is displaced. The phenomenon can be partially explained by the presence of C_{L_q} and $C_{L_{\dot{\alpha}}}$ terms in the lift; however, the fact that the displacement of points has ceased to be more than normal scatter in the upper Mach number region for this and previous models of the series relegates the correction to a position of minor importance.

The lift carpet presenting variation of lift coefficient with Mach number at constant angle of attack is shown in figure 10. Varying model response was such that each angle of attack was not reached over the entire Mach number range of the test.

Figure 11(a) presents the variation of lift-curve slope with Mach number from $M = 0.70$ to $M = 1.37$ for $\delta = -1.99^\circ$. Data are presented for $\delta = 2.07^\circ$ only above $M = 1.0$. The theoretical lift-curve slope of wing alone at supersonic speeds computed from reference 6 is shown for comparison with the C_{L_α} of wing plus fuselage. Wing-plus-fuselage lift-curve slope was calculated by estimating the downwash and subtracting the lift of the tail from the total lift. The lift-curve slope of wing plus fuselage is approximately 95 percent of the theoretical lift-curve slope for wing alone of a comparable triangular wing at supersonic speeds. The lift-curve slope of the modified triangular wing plus fuselage is approximately 22 percent higher at supersonic speeds than the lift-curve slope for an airplane configuration having a 60° triangular wing plus fuselage (reference 7).

Horizontal-tail effectiveness for producing lift is presented in figure 11(b). No data for C_{L_δ} are shown below a Mach number of 1.0

because of the unreliability of the response data at low lift in the subsonic Mach number range. The dashed curve shown for comparison is C_{L_δ} from a previous 60° swept-wing model of the series corrected for the difference in wing area for the two models (reference 3).

Static Stability and Horizontal-Tail Effectiveness

Figure 12 presents the variation of the model period with Mach number. The circles and squares of figure 12 are used to distinguish between periods for the two horizontal-tail deflections and indicate the agreement between periods for the two angle-of-attack ranges covered by the oscillations at each tail position. For the Mach number region below $M = 0.95$ only periods for the high angle-of-attack range are presented.

The variation of the static-stability derivative C_{m_α} with Mach number is shown in figure 13. There were no nonlinearities in C_{m_α} present in the supersonic region as can be surmised from the agreement of periods for the two angle-of-attack regions. No statement can be made about the presence of nonlinearities in the subsonic Mach number region. The C_{m_α} as obtained from the periods of the oscillation showed little changes in going from subsonic to supersonic Mach numbers.

Figure 14 presents the slope of the coefficient of moment for horizontal-tail deflection in the supersonic Mach number region. The horizontal-tail-effectiveness curve was derived from the C_{m_α} curve by multiplying by $(\alpha/\delta)_T$.

Figure 15 presents the position of the aerodynamic center as a function of the Mach number. The curve is for the complete model and exhibits a maximum rearward movement in aerodynamic-center position of 14 percent mean aerodynamic chord in going from subsonic to supersonic Mach numbers. The most forward position of aerodynamic center for the complete configuration was 51.5 percent mean aerodynamic chord at a Mach number of 0.75.

Damping in Pitch

The time to damp to one-half amplitude is shown in figure 16 as a function of Mach number. Figure 17 presents the variation of the sum of the damping-moment derivatives $\left(C_{m_q} + C_{m_{\dot\alpha}}\right)$ with Mach number. The

dip in the curve of $T_{1/2}$ between $M = 1.05$ and $M = 1.20$ and the corresponding reflection in the $\left(C_{m_q} + C_{m_{\dot{\alpha}}}\right)$ curve is unusual. It is noted that the erratic behavior is in the region where the Mach cones from the vicinity of the wing tips include the horizontal tail and is possibly some interference effect. Other than the erratic behavior already noted, the damping variation with Mach number is smooth. The change in damping from $M = 0.80$ to $M = 0.88$ is similar to the change occurring on a model having a 60° swept wing from $M = 0.78$ to $M = 0.88$ which is reported in reference 3.

Longitudinal Trim

Figure 18(a) presents trim angle of attack as a function of Mach number. The upper curve gives the trim α for $\delta = -1.99^{\circ}$ as approximately constant at 2.1°. The maximum subsonic trim change for the negative elevator position is 0.85° and occurs between the Mach numbers of 0.93 and 1.00. The supersonic trim α for $\delta = 2.07^{\circ}$ is approximately constant at -0.50°.

Figure 18(b) presents the variation of trim lift coefficient with Mach number. The drop in trim C_L for $\delta = -1.99^{\circ}$ between $M = 0.71$ and $M = 0.88$ is a result of the drop in lift-curve slope for the corresponding Mach number region. The changes in trim C_L for the supersonic Mach number region are a result of the combination of decrease in trim α and lift-curve slope as Mach number increases. The change in trim C_L for $\delta = 2.07^{\circ}$ is primarily due to the change in lift-curve slope since the trim angle of attack for the supersonic region is approximately constant.

Drag

Curves of total drag coefficient against Mach number for model B and a wingless zero-lift-drag configuration are shown in figure 19(a). The subsonic drag coefficient of model B was 0.0075 with the drag rise occurring at a Mach number of 0.96. The supersonic drag coefficient was almost constant at 0.015 for the zero-lift-drag model. A dip in the drag-coefficient curve occurred at a Mach number of 0.96 as shown by the telemeter test points. This dip has occurred on similar models and may be the result of favorable wing-body interference. Drag rise of the wingless model occurred at a Mach number of 0.98.

In order to obtain the wing-plus-interference drag coefficient shown in figure 19(b) the drag coefficient of the wingless model was subtracted from the drag coefficient of model B. Due to the fact that model B had

two fins and the wingless model had four fins, a correction for the difference in fin drag was made. Base pressure measurements on model B and the wingless model gave different base drag coefficients for the models. Base drag was subtracted from total drag of each model before the subtraction to determine the drag of wing plus interference was made. The wing-plus-interference drag coefficient as obtained from model B was approximately 0.0035 at subsonic speeds. A drag rise occurred in the transonic speed range and a peak drag coefficient of 0.0123 for wing plus interference was reached at a Mach number of 0.98. The wing-plus-interference drag coefficient varies from 0.0080 to 0.0095 at supersonic speeds. Comparisons for wing alone indicate that the minimum drag coefficient of the modified wing tested would be approximately the same as the minimum drag coefficient for an unmodified triangular wing of comparable thickness. Comparisons were made with the 3-percent-thick, 60° triangular wing of reference 8 and a 6-percent-thick, 60° triangular wing from reference 9.

The variation of minimum drag coefficient with Mach number for the stability model is presented in figure 20(a). The early drag rise, which occurs at $M = 0.90$, and the high level of the drag coefficient indicate the unsuitability of this model for determining the minimum drag of respective components. The difficulty in measuring wing drag is accentuated by the low ratio of wing area to fuselage cross-sectional area.

The derivative dC_D/dC_L^2 for the stability model is presented as a function of Mach number in figure 20(b). Figure 20(b) also shows plots of $\frac{1}{57.3} C_{L_\alpha}$ and wing-alone theoretical minimum dC_D/dC_L^2 from reference 10 for the purpose of comparison. The relative placement of the dC_D/dC_L^2 curve between the boundary curves is an indication of the efficiency of the wing in maintaining leading-edge suction. It is to be noted that the wing efficiency itself should be higher than indicated by the relative position of the curves since only the exposed leading edge can contribute to the reduction of drag due to lift.

Typical drag polars for Mach numbers of 0.70, 1.11, and 1.24 are presented in figure 21 for the stability model. From these and similar plots where it was possible, the maximum values of lift-drag ratio and the value of C_L for $(L/D)_{max}$ were established.

Figure 22(a) gives the variation of $(L/D)_{max}$ with Mach number, and the variation of C_L for maximum lift-drag ratio is shown in figure 22(b). The test-limit C_L is also shown in figure 22(b). The Mach number at which the test-limit curve crosses the curves for model A

and model B defines the regions of experimental and extrapolated values for figure 22.

The lower curve of figure 22(a) is for model A. Below a Mach number of 0.94 the values of $(L/D)_{max}$ are measured from drag polars. For Mach numbers of greater than 0.94 the values of $(L/D)_{max}$ are obtained by straight-line extrapolation of the values of (dC_D/dC_L^2) to the C_L for maximum lift-drag ratio.

The curve of $(L/D)_{max}$ shown for model B was calculated by using the zero-lift drag for the drag model and values of dC_D/dC_L^2 from the data for model A. The validity of the assumption that dC_D/dC_L^2 for model A is applicable to model B has not been confirmed experimentally for the two different configurations. It is to be noted that the values of dC_D/dC_L^2 used to calculate the $(L/D)_{max}$ of model B are within the range of lift coefficients obtained in the test of model A and hence are measured values.

The higher values of $(L/D)_{max}$ for model B as compared with the values of $(L/D)_{max}$ for model A are a result of the lower minimum drag of model B. The subsonic value of $(L/D)_{max}$ on model A was approximately 8.4 as compared with a value of approximately 11 for model B. The supersonic value for model A was approximately 5.1 as compared with an approximate value of 9.3 for model B. The decrease in zero-lift drag also reduces the C_L for $(L/D)_{max}$ as is shown by the different level of the two curves in figure 22(b). The high value of lift-curve slope and the realization of some reduction in drag due to lift by leading-edge suction are contributing factors in the performance exemplified by the L/D ratios of the modified wing.

CONCLUSIONS

Free-flight stability and drag tests were made using rocket-propelled models equipped with a modified triangular wing. The wing had an aspect ratio of 2.53 with a 3.7-percent-thick root section and 5.98-percent-thick section at the tip. Results from data analysis indicate the following:

1. The lift-curve slope of wing plus fuselage approached the theoretical lift-curve slope for wing alone at supersonic speeds.

2. The static-stability derivative varied smoothly from subsonic to supersonic Mach numbers.

3. Nonlinearities in the variations of lift and moment with angle of attack were not present at supersonic Mach numbers for the range of lift coefficients tested.

4. Minor trim changes were encountered in the transonic Mach number region.

5. The most forward position of aerodynamic center for the complete configuration was 51.5 percent mean aerodynamic chord at subsonic Mach numbers and maximum rearward movement was 14.0 percent of the mean aerodynamic chord.

6. The minimum drag coefficient for wing plus interference was 0.0035 at subsonic speeds and 0.0080 at supersonic speeds. The peak drag value for wing plus interference was 0.0123 near a Mach number of 1.0. No significant change in minimum-drag characteristics was attributed to the wing modifications.

7. Induced drag for the wing was lowered by the realization of some leading-edge suction.

8. The high lift-curve slope was considered to be a significant change attributable to the wing modifications.

Langley Aeronautical Laboratory
    National Advisory Committee for Aeronautics
        Langley Field, Va.

REFERENCES

1. Gillis, Clarence L., Peck, Robert F., and Vitale, A. James: Pre-
   liminary Results from a Free-Flight Investigation at Transonic and
   Supersonic Speeds of the Longitudinal Stability and Control Char-
   acteristics of an Airplane Configuration with a Thin Straight Wing
   of Aspect Ratio 3. NACA RM L9K25a, 1950.

2. Morrow, John D., and Katz, Ellis: Flight Investigation at Mach Num-
   bers from 0.6 to 1.7 to Determine Drag and Base Pressures on a
   Blunt-Trailing-Edge Airfoil and Drag of Diamond and Circular-Arc
   Airfoils at Zero Lift. NACA RM L50E19a, 1950.

3. Vitale, A. James, McFall, John C., and Morrow, John D.: Longitudinal
   Stability and Drag Characteristics at Mach Numbers from 0.75 to
   1.5 of an Airplane Configuration Having a 60° Swept Wing of Aspect
   Ratio 2.24 As Obtained from Rocket-Propelled Models. RM L51K06,
   1952.

4. Nelson, Robert L.: Large-Scale Flight Measurements of Zero-Lift Drag
   at Mach Numbers from 0.86 to 1.5 of a Wing-Body Combination Having
   a 60° Triangular Wing with NACA 65A003 Sections. NACA RM L50D26,
   1950.

5. Mitchell, Jesse L., and Peck, Robert F.: An NACA Vane-Type Angle-of-
   Attack Indicator for Use at Subsonic and Supersonic Speeds. NACA
   RM L9F28a, 1949.

6. Ribner, Herbert S., and Malvestuto, Frank S., Jr.: Stability Deriv-
   atives of Triangular Wings at Supersonic Speeds. NACA Rep. 908,
   1948. (Formerly NACA TN 1572.)

7. Mitcham, Grady L., Crabill, Norman L., and Stevens, Joseph E.: Flight
   Determination of the Drag and Longitudinal Stability and Control
   Characteristics of a Rocket-Powered Model of a 60° Delta-Wing Air-
   plane from Mach Numbers of 0.75 to 1.70. NACA RM L51I04, 1951.

8. Schult, Eugene D.: Comparison of Large-Scale Flight Measurements of
   Zero-Lift Drag at Mach Numbers from 0.9 to 1.7 of Two Wing-Body
   Combinations Having Similar 60° Triangular Wings with NACA 65A003
   Sections. NACA RM L50I22, 1950.

9. Langley Pilotless Aircraft Research Division: Some Recent Data from
   Flight Tests of Rocket-Powered Models. NACA RM L50K24, 1951.

10. Puckett, A. E., and Stewart, H. J.: Aerodynamic Performance of
    Delta Wings at Supersonic Speeds. Jour. Aero. Sci., vol. 14, no. 10,
    Oct. 1947, pp. 567-578.

TABLE I

INSTRUMENTATION

Stability Model

Quantity	Full-scale instrument range	0.01 full-scale range	Typical quantity per 0.0055-inch record trace
Angle of attack, α	18.20	0.182	0.039
Longitudinal acceleration, a_l/g	7.00	0.07	0.016
Normal acceleration (sensitive), a_n/g . . .	20.00	0.20	0.060
Normal acceleration (high-range), a_n/g . . .	45.00	0.45	0.095
Transverse acceleration	8.00	0.08	0.0099
Control position, δ . . .	4.08	0.04	0.0076
Pressure, total head, psi	46.00	0.46	0.0057
Pressure, body orifice, psi	6.00	0.06	0.0039

Drag Model

Quantity	Full-scale instrument range	0.01 full-scale range
Longitudinal (positive) acceleration, a_l/g . .	20.00	0.20
Longitudinal acceleration, a_l/g	5.00	0.05
Longitudinal acceleration, a_l/g	5.00	0.05
Pressure, base, psi . .	10.00	0.10

50.66°

57.08°

24.38

8.09

3.23

17.00

1.0

7.69

0.25 M.A.C.

0.25 M.A.C.

33.86

47.15

30.35

10.00

13.75

7.75

B

B

17.00

7.00

AA

10.63

39.28

84.00

90.25

BB

NACA

Typical fin sections
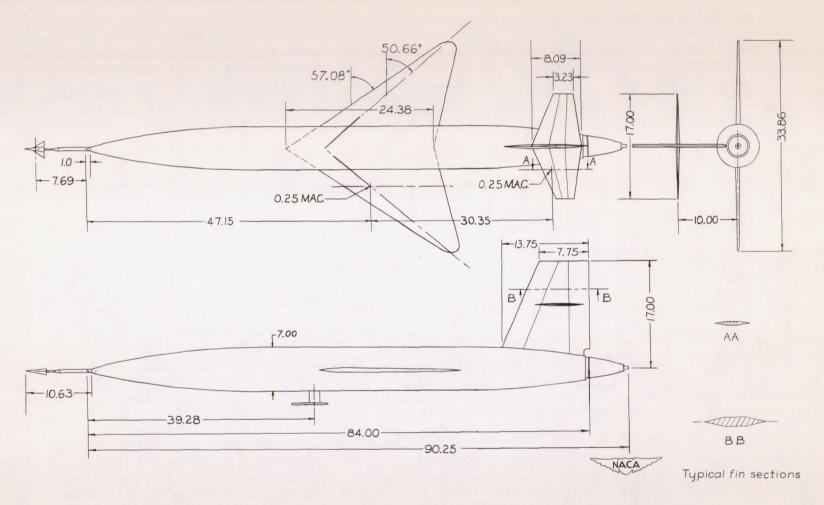
Figure 1.- General arrangement of stability model. All dimensions are
in inches.
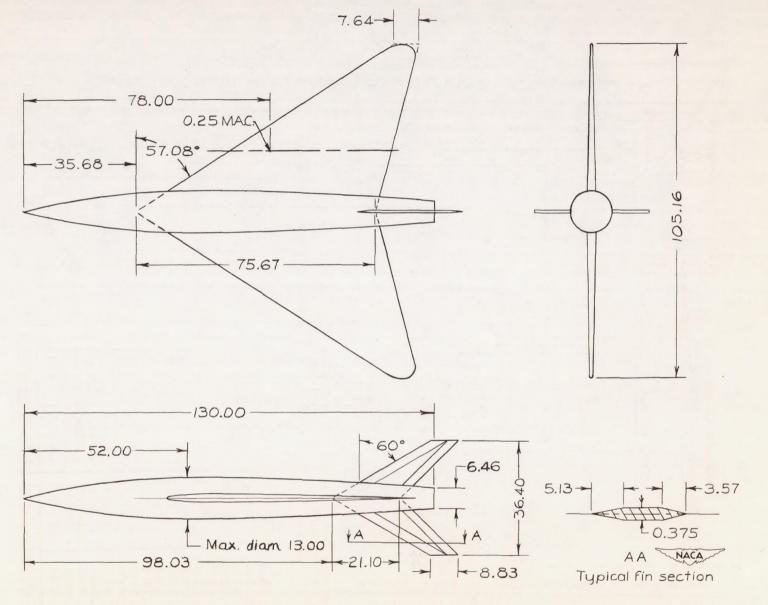
Figure 2.- General arrangement of minimum-drag model. All dimensions are in inches.

Y

Maximum thickness

Point of convergence

X

.0616

.0308

.1103 R

.0488 R

.1103 R

B

B

.0660

.2207

.6018

.5509

.6945

.9615

.8138

57.08° A

.1505

14.08° A

1.000

.4495

Airfoil at A-A

COORDINATES AT A-A	
X	Y
0.00000	0.00000
.00628	.00476
.01255	.00656
.02506	.00890
.03762	.01054
.05017	.01173
.07523	.01341
.1003	.01440
.1254	.01489
.1505	.01505
.3713	.01456
.5006	.01329
.5928	.01144
.6637	.00919
.7221	.00656
.7705	.00365
.8136	.00033
L.E. RAD.-.0016	

COORDINATES AT B-B	
X	Y
0.00000	0.00000
.00275	.00209
.00554	.00287
.01214	.00394
.01657	.00464
.02207	.00517
.03310	.00591
.04414	.00632
.05517	.00656
.06621	.00660
.08828	.00640
.11038	.00582
.13245	.00505
.15452	.00406
.17659	.00291
.19866	.00160
.22073	.00012
L.E. RAD.-.0009	

Maximum thickness

Airfoil at B-B

Note: Drawing nondimensional factor is chord through wing apex.

NACA

Figure 3.- Wing detail drawing.

(a) Top view.

L-66936.1
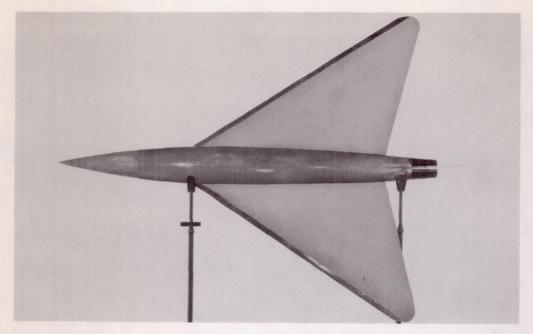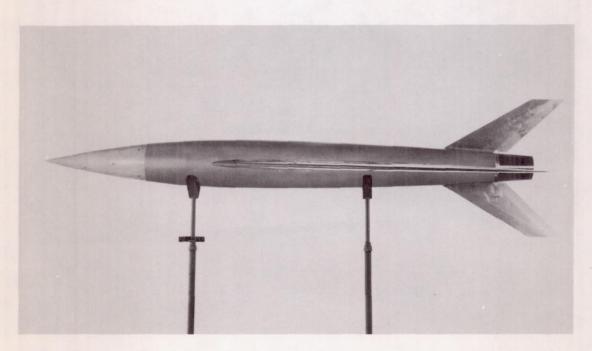
(b) Oblique three-quarter front view.

L-66937.1

Figure 4.- Photographs of longitudinal-stability model.

(a) Plan view.   L-69267.1

(b) Side view.   L-69266.1

Figure 5.- Photographs of drag model.
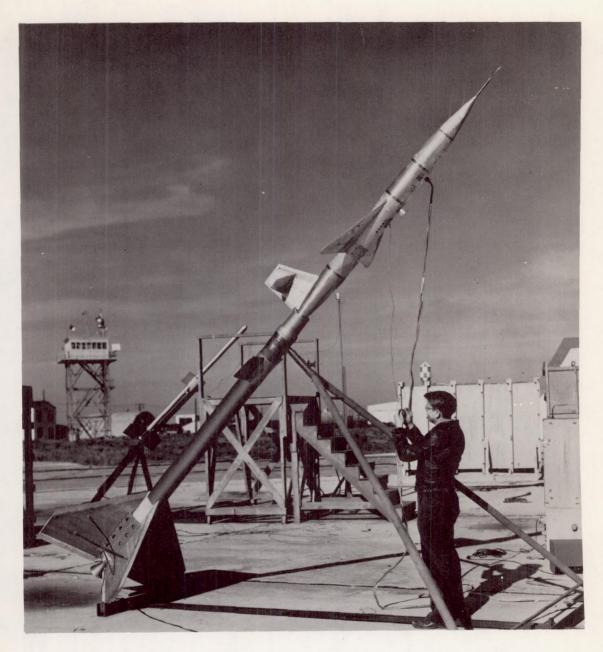
Figure 6.- Launching photograph of stability model.

L-67848.1
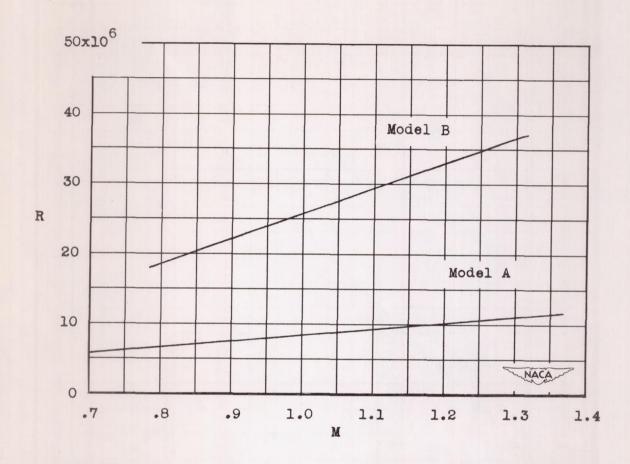
Figure 7.- Variation of Reynolds number with Mach number for test models. Reynolds number based on wing mean aerodynamic chord.
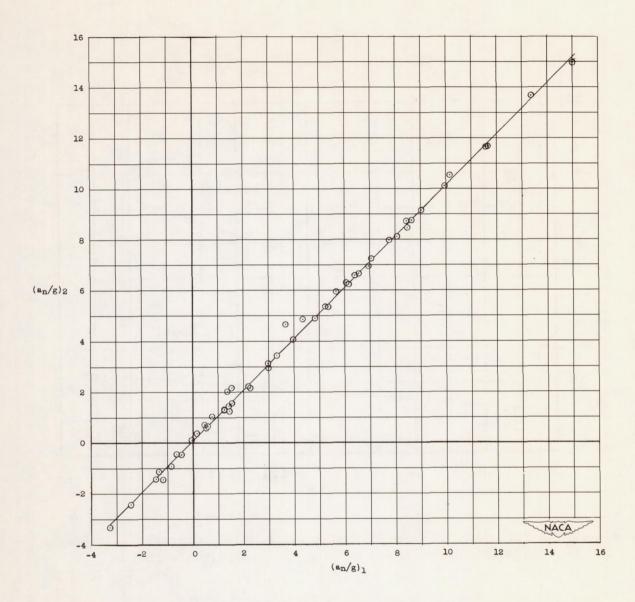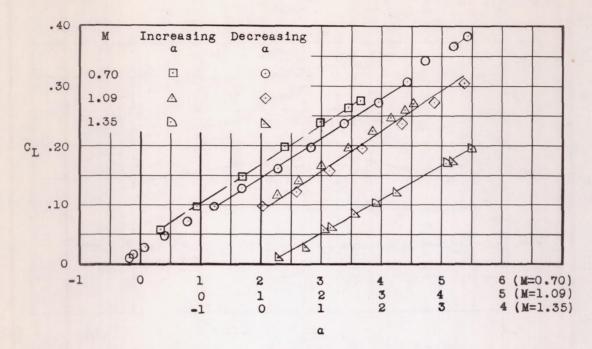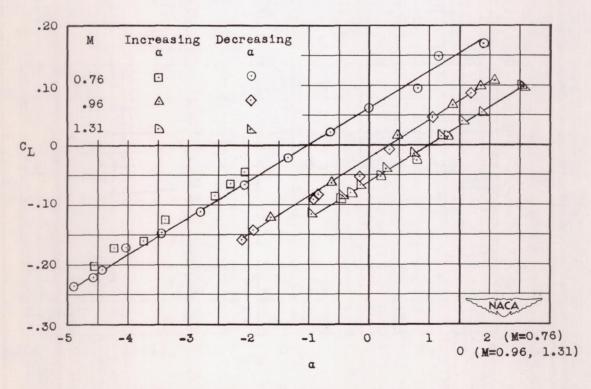
Figure 8.- Correlation of normal accelerations. High-range readings
plotted as a function of low-range readings.
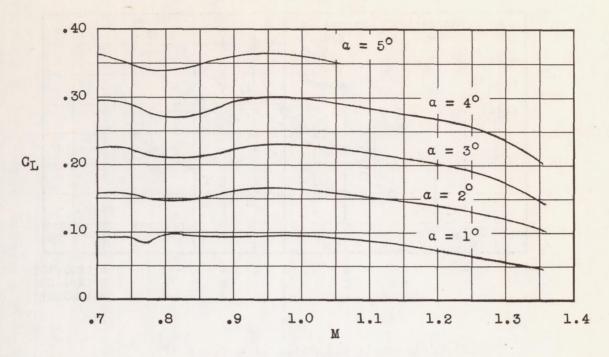
(a) Horizontal-tail deflection of -1.99°.
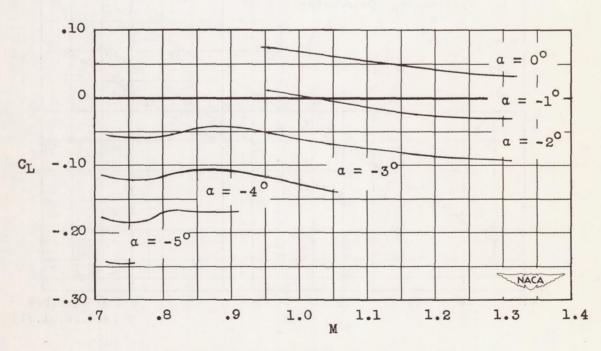
(b) Horizontal-tail deflection of 2.07°.

Figure 9.- Typical variation of lift coefficient with angle of attack
for the stability model.
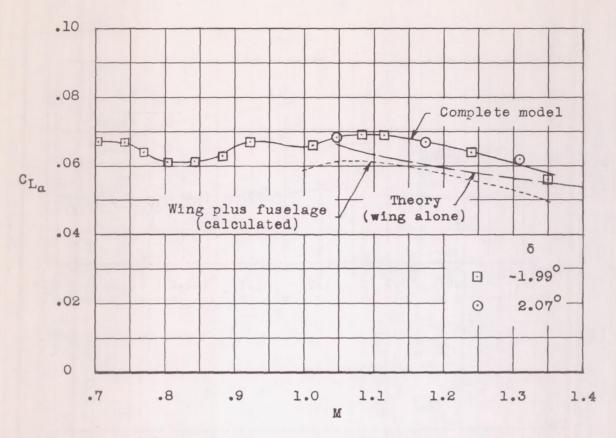
(a) Elevator deflection of -1.99°.
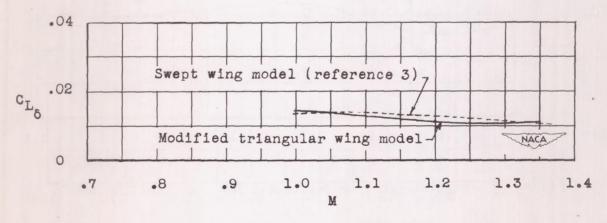
(b) Elevator deflection of 2.07°.

Figure 10.- Variation of lift coefficient with Mach number.

(a) Lift-curve slope for angle of attack.

(b) Lift-curve slope for elevator deflection.

Figure 11.- Lift-curve slopes for the stability model.
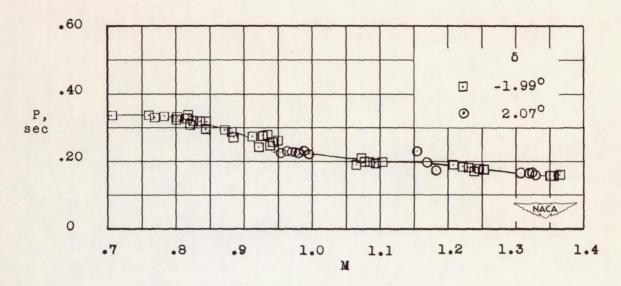
Figure 12.- Period of the transient oscillation for the stability model.
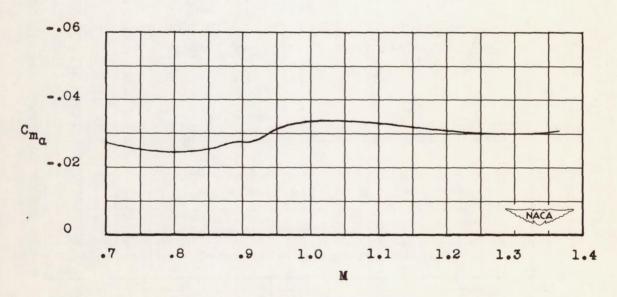
Figure 13.- Static-stability derivative for the stability model.
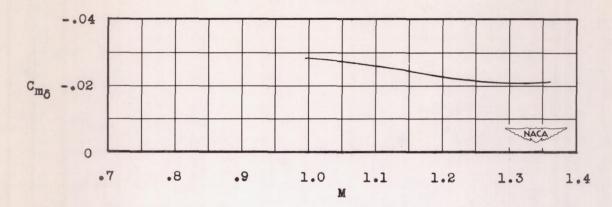
Figure 14.- Horizontal-tail effectiveness for producing pitching moment.
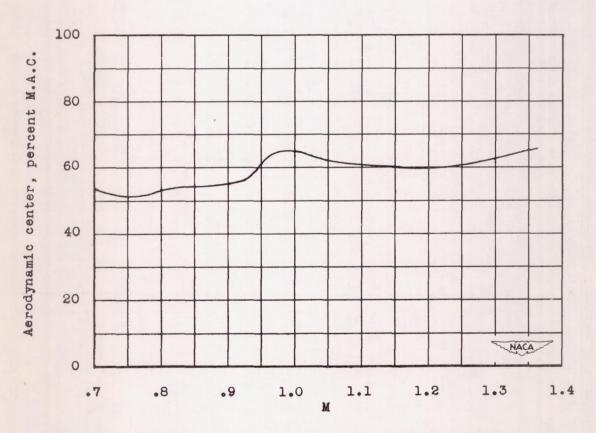
Figure 15.- Aerodynamic-center location for the stability model.
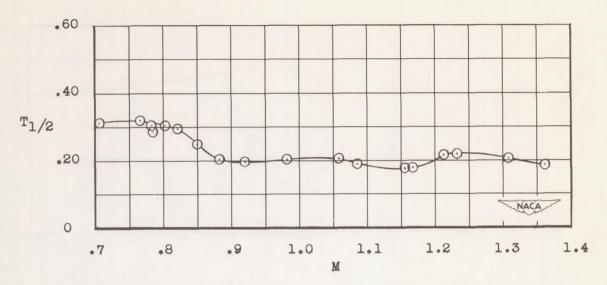
Figure 16.- Time to damp to one-half amplitude.
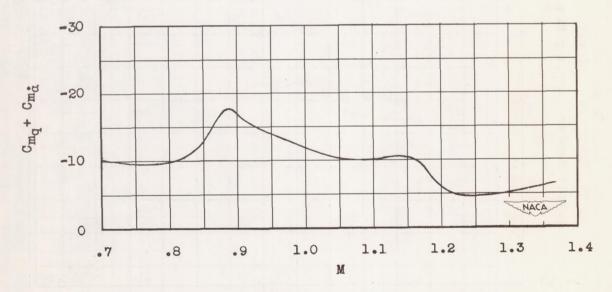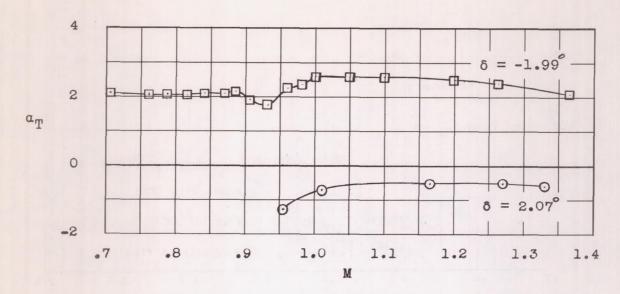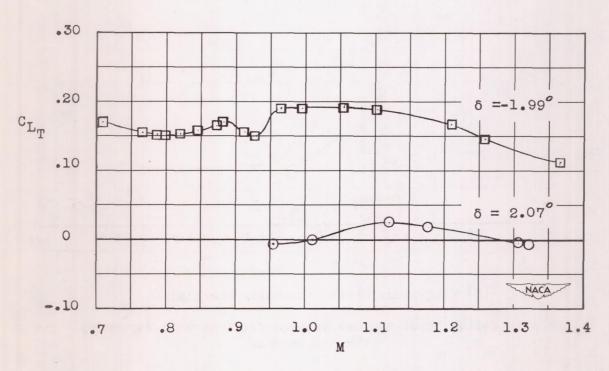
Figure 17.- Damping derivatives for the stability model.
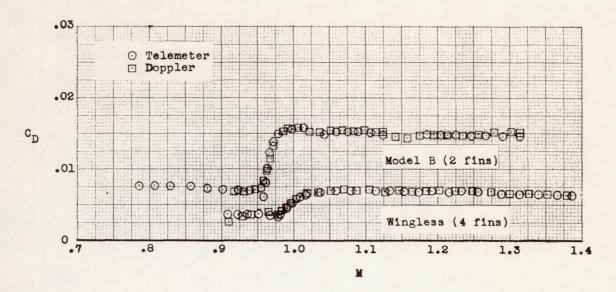
(a) Trim angle of attack.
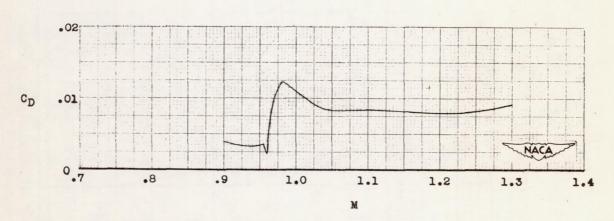
(b) Trim lift coefficient.

Figure 18.- Trim characteristics of the stability model.
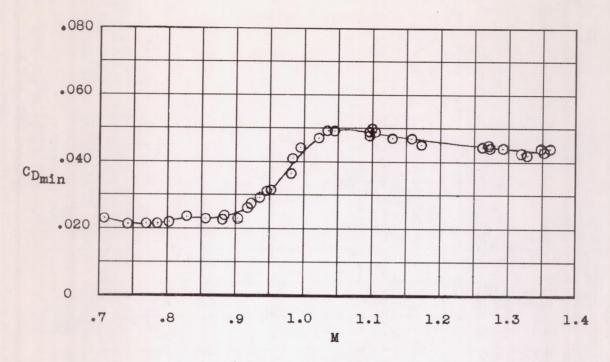
(a) Total drag coefficient.
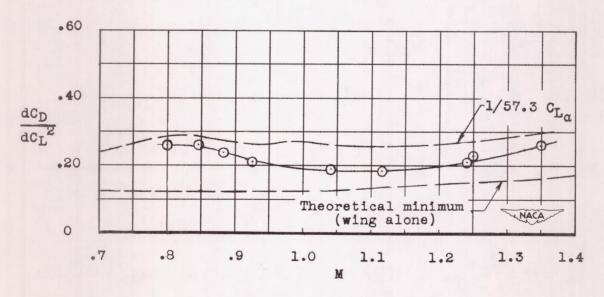
(b) Wing-plus-interference drag coefficient.

Figure 19.- Variation of minimum drag coefficient with Mach number for the drag model.

(a) Minimum drag.

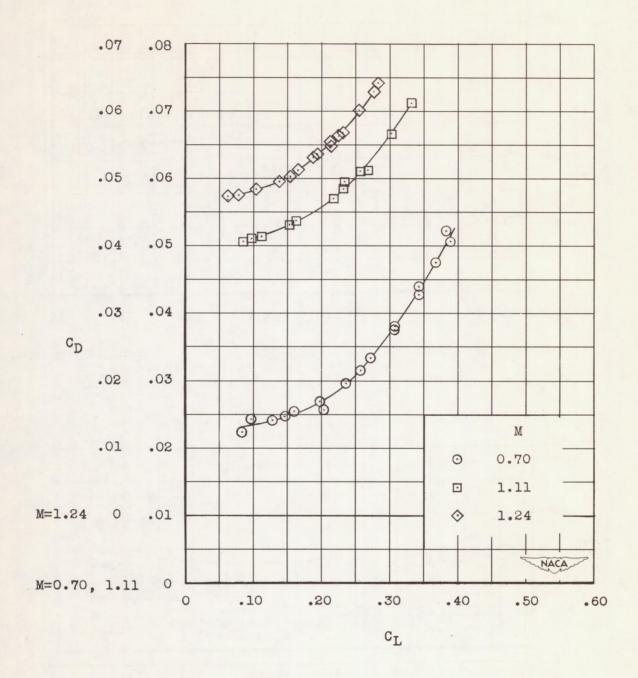(b) Induced drag.

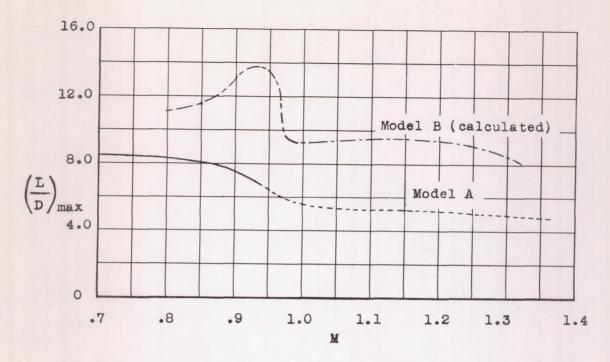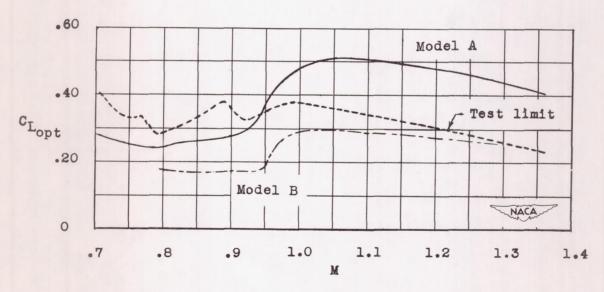Figure 20.- Drag characteristics of the stability model.

Figure 21.- Typical variation of drag with lift for the stability model.

(a) Maximum ratio of lift to drag.

(b) Lift coefficient for maximum ratio of lift to drag.

Figure 22.- Characteristics of lift-drag ratio.